NUMERICAL STUDY OF INTERFERENCE EFFECTS OF WING-MOUNTED ADVANCED ENGINE CONCEPTS

C.-C. Rossow, H. Hoheisel

DLR, Institut für Entwurfsaerodynamik
Lilienthalplatz 7, D-38108 Braunschweig, Germany

Abstract

The aerodynamic interference effects of three different wing mounted engine concepts, namely a conventional turbofan, a very high by-pass ratio turbofan, and an ultra high by-pass ratio ducted propfan are investigated by the solution of the Euler equations. Due to the interference of fan jet and wing, the ultra high by-pass engine shows the largest interference. A variation of position reveals for both the very high and the ultra high by-pass ratio engine a potential for a close coupling of engine and airframe.

1. Introduction

The aerodynamic performance of an aircraft has great influence on the fuel consumption, and therefore strongly affects the emissions of the propulsion system. In order to reduce emissions for an enhanced environmental compatibility it is necessary to increase the lift to drag ratios of advanced future aircrafts. Furthermore, the propulsive efficiency of state-of-the art turbofans has still a large potential of improvement, which may be realized by significantly increasing the by-pass ratio (perhaps from 5 up to 15) [1] .

However, the higher by-pass ratios require larger fan diameters, and care has to be taken that the interference effects caused by the installed engine do not degrade the aerodynamic performance too severely. Therefore, airframe / engine-integration becomes a key technology in the design and development of advanced aircraft. For wing-mounted engines the problem is additionally aggravated by the fact that the larger engine diameters and the restrictions placed by the available length of the landing gear require a closer coupling of engine and wing.

Recently, numerical methods are more and more used to gain insight into the elements playing a role in the interference process [2] , [3] . It has been shown that already the solution of the Euler equations is capable of predicting essential effects caused by the installation of an engine [4] . When solving the Euler equations viscous effects may efficiently be estimated by considering the displacement thickness of the boundary layer on the wing [5] . Provided a flexible grid generation procedure is established, a numerical method allows the efficient investigation of different engine concepts and different engine locations. The influence of the propulsion concept on the aerodynamics of the airframe may be studied, and positions causing too strong effects on the flow around the wing may be identified.

In the present contribution, the interference effects of three different engine concepts, namely a conventional turbofan engine, a very high by-pass ratio turbofan, and an ultra high by-pass ducted propfan are assessed. The special configuration considered here is a twin engine Airbus-type aircraft. The geometry of the wing body combination corresponds to the DLR-ALVAST wind tunnel model. Experimental and theoretical investigations of this wing body combination were carried out for low subsonic speeds [6] . A theoretical investigation for the interference effects of a conventional TF and a UHBR engine on the ALVAST configuration was performed for transonic speeds [7] . The present study establishes a consequent continuation of this work.

Currently, there is a trend towards VHBR engines as the propulsive concept of the near future. Such an engine may be viewed as lying between the conventional turbofan and the UHBR concept. Therefore, it appears appropriate to compare the interference effects of a VHBR engine to those of a TF and a UHBR engine.

Besides the comparison of the three engines, a systematic variation of the position of the VHBR and the UHBR propulsion systems will be performed in order to identify possible aerodynamic limitations for the locations of the engines.

2. Analysis Tool

The investigation of the different engine concepts and influence of different engine positions is carried out by the solution of the Euler equations. With respect to solving the full potential equation, the advantage of the solution of the Euler equations is that mass, momentum, and energy are conserved. Additionally, for the Euler equations the vortex sheet behind a lifting wing needs not to be specified, and the geometry of an inviscid jet comes out as part of the solution. On the other hand, compared to the solution of the Navier-Stokes equations, the effort for the generation of

computational grids and the computer time required for the calculation tends to be an order of magnitude smaller, and essential interference phenomena may already be observed in inviscid flow [4] .

2.1 Solution Scheme

The Euler equations are solved in integral form in order to ensure conservation for the discrete equations. The physical domain around the aerodynamic body is subdivided into hexahedral cells, and the discrete values of the flow quantities are located at the vertices of the mesh cells. Since this discretization leads to central difference approximations, additional artificial dissipative terms are introduced to damp out high frequency oscillations.

Time integration is performed using an explicit 5-stage Runge-Kutta time stepping scheme. Since interest is focussed on steady flow fields only, various techniques, like local time stepping, implicit residual averaging, and multigrid are used to accelerate convergence towards steady state.

The algorithms are implemented in the DLR-code CEVCATS. This code is written in a block-structured form and allows an arbitrary application of boundary conditions on the block faces. Details of the code structure may be found in [8] .

For transonic flows over wings the neglection of viscous effects leads to a systematic error when comparing the solutions to experimental results [4] . Therefore, in the present study viscous effects are estimated by adding the displacement thickness of the boundary layer to the wing geometry. This concept has been introduced in [9] for wing body configurations, and in [5] the extension for the calculation of interference effects has been shown. The displacement thickness of the wing alone is computed with the FLO22VIS code [10] , which consists of the FLO22 code from Jameson [11] , and the 3D boundary layer integral scheme from Stock [12] . Due to the addition of the displacement thickness the wing geometry is widened and the wing is not closed at the trailing edge. As outlined in [5] , the addition of the displacement thickness moves the shock wave further upstream, and the rear loading is reduced, thereby resembling more closely experimental results.

2.2 Grid Generation

The basis for an investigation like the one intended in this study is a fast and flexible grid generation procedure, which allows an easy change of engine type and position. Here the mesh generation system of [13] is used for the generation of body-fitted, block-structured meshes. The mesh generation system in [13] was especially designed for the generation of grids around transport aircraft with wing mounted engines. The grid topology in this grid generation system is chosen such that a change of engine type or position does not require a change of grid topology. Changes in the grid due to different engine concepts are limited to a confined region around the engine itself. To achieve this, an H-type grid structure in streamwise direction and an O-type structure in spanwise direction is employed for the wing body configuration. Engine and pylon are integrated into this basic grid by introducing a sub-block containing these components. For this purpose a specified region is cut out of the global grid to allow the substitution of the subgrid containing the propulsion components. As a topology for the subgrid around engine and pylon also an H-type structure in streamwise direction is employed, and in circumferential direction with respect to the engine axis a polar grid topology is applied. The outer boundary of the polar subgrid is adapted in order to match the cut out region of the global grid.

A three-dimensional view of the resulting field grid around a wing body combination with conventional turbofan engine is given in Figure 1. The region of the polar subgrid containing the propulsion components can clearly be seen. Note that using the above described mesh topology the global H-O grid around the wing body configuration may be left unchanged when introducing different subgrids for different engine types and locations.

The complete field grid around the wing body configuration with engine and pylon consists of approximately 650,000 mesh cells and 11 computational blocks. The surface mesh on the wing has 40 cells in spanwise direction, and cells are concentrated at the pylon location. 144 cells are used around an airfoil section. For the engine 64 cells have been employed in circumferential direction.

3. Configurations under Investigation

The special configuration considered here is a twin-engine Airbus-type aircraft. The geometry of the wing body combination corresponds to the DLR-ALVAST wind tunnel model [14] , and a sketch of the configuration with an advanced engine is given in Figure 2. Three different types of engines will be investigated, namely

- a conventional turbofan (TF) with a by-pass ratio of $\mu \approx 5$
- a Very High By-pass Ratio (VHBR) engine with a by-pass ratio of $\mu \approx 11$
- a Ultra High By-pass Ratio (UHBR) engine with by-pass ratio of $\mu \approx 23$.

The conventional turbofan engine is scaled in accordance with a CFM-56 engine installed on an Airbus A320. The geometry of the UHBR engine corresponds to the DLR-CRUF simulator [15] , which had been used on the ALVAST model for experimental and theoretical investigations in the framework of the BRITE/EURAM program DUPRIN [16] . The dimensions of the VHBR and UHBR

engines are chosen such that they represent propulsion units with a thrust of about 30,000 lb.

The position of an engine under a wing may be specified by the distances x_F and H, where x_F is the horizontal distance between leading edge point of the wing and upper trailing edge point of the nacelle, and H being the vertical distance between these two points, as sketched in Figure 3. The positions of the three different engines investigated here are given in Figure 3, where the basic position of the engines are denoted by 1. The position of the TF engine is that realized in the experimental investigations of [16] and corresponds to a representative location of a conventional engine. The basic position of the UHBR propulsion unit is also taken from [16] . The interference effects of the two engines at these positions have already theoretically been investigated in [7] for the same transconic flow conditions as will be considered here. Therefore they serve as the basic reference positions. The basic position of the VHBR engine is chosen such that the horizontal distance x_F agrees with that of the turbofan engine, and for the vertical position the engine axis of the VHBR is located at the same position as the UHBR engine.

For all configurations, the pylon is of symmetrical shape. The leading edge of the pylon is defined by a straight line connecting the wing leading edge with the nacelle at a specified chord length. Varying the engine position varies the inclination of the pylon leading edge, however the thickness of the pylon is always kept constant. Thus the influence of a varying pylon shape is kept to the smallest amount possible.

Figure 4 gives a sketch of the three basic engine positions, and in Figure 5 the surface meshes for the three configurations are presented.

4. Results

For the investigations of the interference effects representative cruise conditions are chosen, and the freestream conditions are set to $M_\infty = 0.75$ and $\alpha = 0.84°$. In order to represent engine operating conditions, the incoming mass flow has to be specified at the fan inflow face, and at the engine outflow faces the pressure and temperature ratios have to be prescribed.

The incoming mass flow is given by the stream tube area ratio $\varepsilon_{HL} = \frac{A_0}{A_{HL}}$, with A_0 being the cross-sectional area of the stream tube at infinity, and A_{HL} the area of the nacelle at the highlite position. The outflow conditions are determined by the jet pressure ratio P_{tj}/P_0, where P_{tj} denotes the total pressure in the jet and P_0 is the ambient static pressure, and the temperature ratio T_{tj}/T_{t0} , with T_{tj} being the total jet temperature and T_{t0} the total ambient temperature. In the numerical simulation, the temperature ratio is always set to unity, i.e. only cold jets are simulated. Furthermore, no attempt has been made to simulate the correct by-pass ratio. Instead, at fan and core outflow faces always identical boundary conditions are applied. Table 1 gives the conditions specified in the computation for the different engines.

The presentation of results is split into two parts: First, the three propulsion concepts will be compared at their basic positions. Since a comparison for the TF and UHBR engine was already performed in detail in [7] , here mainly the effects of the VHBR engine will be pointed out. Second, for the VHBR engine and for the UHBR engine a variation of the engine position will be carried out to explore other possible locations and to find limitations in position due to unacceptable interference effects.

4.1 Comparison of Engine Concepts

Figure 6 shows spanwise lift distributions for the ALVAST wing-body combination equipped with the three different engines. The spanwise location of the engine is always kept constant, and the positions with respect to the wing leading edge are those indicated in Figure 3 as VHBR Position 1 and UHBR Position 1. As a reference the lift distribution of the configuration without engines is included in the figure. The installation of the engines leads to a loss of lift over the complete wing surface, as already noted in [4] , [7] . Inboard of the pylon, the installation of the UHBR engine causes a larger decrease of lift than TF and VHBR, for the latter two no differences occur in this region. Outboard of the pylon up to the wing tip, the lift decreases with increasing engine dimensions, i.e. the UHBR engine causes the largest loss in lift, and the lift loss due to the VHBR installation lies between that caused by TF and UHBR.

A more detailed analysis of the interference effects is provided by sectionwise pressure distributions. Pressure distributions will always be shown at a spanwise location closely inboard of the pylon (y/b = 0.33), and one closely outboard of the pylon (y/b = 0.38). The position of the spanwise sections is included in the sketch of Figure 2. To allow a better estimation of the engine interference, Figure 7 shows a comparison for the configuration with turbofan engine and for the clean configuration without engine. In both sections the shock wave is moved further upstream by the engine installation, and in [7] it was pointed out that this effect takes place over the whole spanwidth due to the propagation of disturbances in the supersonic part of the flowfield. On the lower wing surface a distinct difference between the inboard and outboard pressure distribution is observed for the installed case. In [7] this effect has been explained by the distortion of the streamlines on a swept

wing due to the presence of the pylon.

Figure 8 shows the corresponding pressure distributions for the configuration with the three different engines installed. On the upper wing surface a clear trend is observed: increasing the engine dimensions successively from TF to VHBR and to UHBR moves the shock wave more and more upstream. The larger the engine the more the local incidence of the flow relative to the wing at the engine position is reduced. Due to the propagation of disturbances in the supersonic flowfield on the upper wing surface, the local reduction of incidence causes an upstream shift of the shock wave on the whole upper surface, leading to the successively reduced lift distribution outboard of the pylon in Figure 6.

On the lower wing surface TF and VHBR show qualitatively a similar behaviour. However inboard of the pylon for the TF engine the flow is stronger accelerated in the first 30% of the chord as for the VHBR engine. Since the TF engine causes lower pressures as the VHBR engine inboard of the pylon, the lift loss due to the more upstream shift of the shock wave is compensated, as can be seen in the lift distribution of Figure 6. Outboard of the pylon differences between TF and VHBR are only small. The interference effects caused by the UHBR differs significantly from those observed for TF and VHBR, especially inboard of the pylon. Due to the fan jet which passes very closely under the wing, the flow is substantially accelerated and causes a region of very low pressure inboard of the pylon. This low pressure region is responsible for the additional loss of lift inboard of the pylon. Outboard of the pylon the flow acceleration is much less pronounced, however still stronger than for TF and VHBR engines.

Figure 9 shows the Mach number distribution of the flowfield around the configuration with UHBR engine in a cross-section inboard of the pylon location. The inviscid jet can be identified by the concentration of iso-lines at the jet boundaries. Note that due to the numerical dissipation the jet boundaries are not given by crisp discontinuities. The region of strong flow acceleration for the UHBR engine due to the closely passing jet under the wing can clearly be seen in the figure.

4.2 Variation of Engine Position

The higher by-pass ratios necessary to achieve better specific fuel consumption require substantially larger diameters as conventional turbofan engines. Installing these engines on todays aircraft may be prohibited by the available length of the landing gear, since due to the larger dimensions the required off-ground distance may become too small. Therefore, these engines have to be located as closely as possible under the wing. Additionally, the length of the advanced propulsion concepts increases, and it may be desirable to also reduce the horizontal distance to the wing leading edge. Figure 3 gives a view of the different positions investigated in this study. From Ref [17] a boundary has been included for positions where the interference drag becomes not acceptable. This boundary served as a guide line for the selection of the positions being investigated here. In Table 2 the different geometrical parameters of the engines and their positions are summarized.

Variation of the VHBR Position

As already mentioned, the basic position of the VHBR engine, denoted as Position 1, is defined by the same horizontal distance x_F as realized for the turbofan engine. The vertical distance H of Position 1 was chosen such that the axis of the VHBR coincides with the axis of the UHBR engine given in Ref. [16] , see Table 2.

In order to establish a closer coupling of engine and wing, first the vertical distance H was reduced such that H is identical for turbofan and VHBR, yielding Position 2. For Position 3 the location of the axis of the VHBR was required to be identical with the axis of the basic turbofan. With this further reduction the position is very close to the boundary line indicated in Figure 3. Note that the horizontal distance for Positions 1, 2, and 3 is identical.

In Figure 10 the spanwise lift distribution for the three positions is displayed. The differences caused by the geometrical variation are only marginal. The reason for this somewhat surprising result may be found when regarding the pressure distributions in Figure 11. A clear trend may be observed: moving the engine closer to the wing leads to a more and more upstream shift of the shock wave on the upper wing surface. On the lower wing surface, the flow is less accelerated when moving the engine closer to the wing. This behaviour is observed in both spanwise sections. Concerning the lift distribution, these two effects counter-balance each other: the loss of lift due to the upstream shift of the shock is compensated by the pressure gain on the lower surface. The main result of the vertical variation is that a closer coupling of VHBR and wing does not severely deteriorate the aerodynamics of the wing.

The axial length of the VHBR engine substantially exceeds the length of the turbofan engine. For the same horizontal position x_F of the nacelle trailing edge, the leading edge of the VHBR engine is located far more upstream than that of the turbofan. At this horizontal position, the leading edge of the VHBR is even located further upstream than the leading edge of the UHBR at its basic position. It therefore may be desirable to also realize a closer coupling in horizontal direction. Based on the vertical distance of Position 3, the VHBR engine is horizontally moved closer to the wing into Position 4, see Figure 3. At this position, the trailing edge point of the nacelle lies downstream of the wing leading edge. Figure 12 gives a comparison of the

spanwise lift distributions calculated for Position 3 and Position 4. Inboard of the pylon, Position 4 leads to a loss of lift, whereas outboard differences are negligible.

The pressure distributions in Figure 13 show that the downstream shift of the engine position reduces the influence on the upper wing surface, since the shock wave also moves further downstream. On the lower wing surface, the influence of the propulsion system is now however more pronounced. Inboard of the pylon, the flow is strongly accelerated due to the location of the nacelle trailing edge downstream of the wing leading edge. The downstream position of the engine changed the cross-section of the duct formed by nacelle, pylon and wing, and thus aggravated the channel effect responsible for the flow acceleration the first 15% of the chord length. Further downstream the flow is decelerated with respect to Position 3. Outboard of the pylon, the same tendency is observed, however the effect is not that strong as on the inboard side. Compared to Position 3, the interference caused by Position 4 tends to be more severe. It is however instructive to compare the pressure distribution of VHBR Position 4 with those of the basic turbofan, as done in Figure 14. Both configurations show a very similar behaviour, and with respect to the turbofan, even the interference effects of the VHBR at Position 4 appear to be acceptable. This is confirmed by the comparison of lift distributions in Figure 15.

Variation of the UHBR Position

The basic position of the UHBR engine was defined in [16]. Since the leading edge of the nacelle is located further upstream compared to the turbofan engine, the UHBR engine is moved successively closer to the wing in horizontal direction. This variation is given by the UHBR Positions 2 and 3 in Figure 3. The backward shift of the engine shows a clear trend in the spanwise lift distributions displayed in Figure 16. Moving the engine closer to the wing continuously reduces the lift. The pressure distributions in Figure 17 also show a clear dependency on the engine location: the more downstream the position, the more the flow is accelerated on the lower wing surface. This holds especially for the inboard side of the pylon, where the jet effect is quite strong for Position 1 already. Shifting the engine downstream decreases the pressure even further, and the resulting pressure gradients may become too unfavourable. On the upper wing surface, the influence of the variation of position is negligible.

Regarding the large diameter of the UHBR engine, a reduction of the vertical distance to the wing is desirable. Based on the horizontal location of Position 1, the axis of the UHBR engine is moved to the position of the axis of the VHBR engine at VHBR Position 2.

This new position is referenced as UHBR Position 4. Figure 18 presents a comparison of the results from Positions 1 and 4. The lift distribution for the two positions is almost identical, and so are the pressure distributions, not presented here. This shows that there is still a potential to locate the UHBR engine closer to the wing in vertical direction. This will alleviate the problems associated with the installation of such engines, also with respect to the strong influence of viscous jet effects observed during the investigations of [16].

5. Conclusion

The interference effects of a twin engine transport aircraft with different propulsion concepts have been investigated numerically. The analysis has been performed by solving the Euler equations using the DLR-code CEVCATS. Viscous effects have been considered by adding the displacement thickness of the boundary layer to the wing geometry. The geometry of the wing body combination investigated was given by the DLR-ALVAST wind tunnel model. The first part of the study dealt with the comparison of the interference effects of a conventional turbofan engine, a VHBR engine, and a UHBR engine. In the second part of the study the positions of VHBR and UHBR engine were systematically varied to explore limitations for the location of the engines. The analysis lead to the following results:

- At their basic positions, TF and VHBR engine show similar interference effects. The effect of the more upstream shift of the shock wave by the VHBR engine is compensated by the less accelerated flow on the lower surface, compared to the turbofan engine. The UHBR engine shows the most upstream shift of the shock wave, and on the lower wing surface the fan jet of the UHBR engine causes a significant region of low pressure.
- The variation of the VHBR position showed a relatively small effect when reducing the vertical distance to the wing. Taking the vertically closest position and shifting the engine downstream increased the interference effects, but they are still comparable to those caused by the basic turbofan.
- The variation of the UHBR position revealed that shifting the engine downstream severely increased the jet interference with the wing and enlarged the low pressure region on the wing lower surface. However, taking the basic upstream position and moving the engine vertically closer to the wing had essentially no effect. This may alleviate the problems encountered by the technical installation of such engines.

References

[1] Rech, J.
Integration sur avion des ensembles propulsifs futurs.
Colloque AERO PROPULSION 1990 at Paris, France, 1990.

[2] Rill, S.; Becker, K.
Simulation of Transonic Inviscid Flow over a Twin Jet Transport Aircraft.
AIAA 91-0025, 1991.

[3] Naik, D.
3-D Euler Calculations for Aft-Propfan Integration
AIAA 90-2147, 1990.

[4] Rossow, C.-C.; Godard, J.-L.; Hoheisel, H.; Schmitt, V.
Investigation of Propulsion Airframe Integration Interference Effects on a Transport Aircraft Configuration.
AIAA 92-3092, 1992.

[5] Brodersen, O.; Rossow, C.-C.
Calculation of Interference Phenomena for a Transport Aircraft Configuration Considering Viscous Effects.
European Forum Conference on Recent Developments and Applications in Aeronautical CFD, Bristol, GB, Sept. 1993.

[6] Hoheisel, H.; Kiock, R.; Rossow, C.-C.; Ronzheimer, A.; Baumert, W.; Capedevila, H.
Aspects of Theoretical and Experimental Investigation of Airframe/Engine Integration Problems.
ICAS-Congress, Paper 90-2.7.3, 1990.

[7] Rossow, C.-C.; Ronzheimer, A.
Investigation of Interference Phenomena of Modern Wing-Mounted High-Bypass-Ratio Engines by the Solution of the Euler-Equations.
AGARD Symposium on 'Aerodynamic Engine/Airframe Integration', Fort Worth, USA, 1991.

[8] Atkins, H. L.
A Multi-Block Multigrid Method for the Euler and Navier-Stokes Equations for Three-Dimensional Flows.
AIAA 91-0101. 1991.

[9] Wichmann, G.
Ein Verfahren zur Berechnung der Umströmung von Flügel-Rumpf-Konfiguration unter Berücksichtigung der Tragflügelgrenzschicht.
DGLR Report 90/06, 1990.

[10] Wichmann, G.
Ein schnelles Verfahren zur Bestimmung des Reibungseinflusses bei Flügeln großer Streckung.
STAB-Workshop, Göttingen, FRG, 1989.

[11] Jameson, A.; Caughey, P.A.
Numerical Calculation of the Transonic Flow past a swept wing.
ERDA report C00-3077-140, New York University, 1977.

[12] Stock, H. W.
Integral Method for the Calculation of Three-Dimensional Laminar and Turbulent Boundary Layers.
NASA TM 75320, 1978.

[13] Rossow, C.-C.; Ronzheimer, A.
Multi-Block Grid Generation Around Wing-Body-Engine-Pylon Configurations.
Proceedings of 3rd International Conference on Numerical Grid Generation in Computational Fluid Dynamics and Related Fields, Barcelona, Spain, 1991.

[14] Redeker, G.
Modelldefinition für ein Verkehrsflugzeug im Rahmen des zukünftigen Programms ALVAST.
DLR-IB 151-80/13, 1980.

[15] Hoheisel, H.
The Design of a Counter Rotating Ultra-High-Bypass Fan Simulator for Windtunnel Investigations
DLR-FB 93-20 (1993).

[16] Burgsmüller, W.; Hoheisel, H.; Kooi, J. W.
Engine/Airframe Interference on Transport Aircraft with Ducted Propfans- The European Program DUPRIN-
ICAS-Paper-94-6.2.1, ICAS-Congress Anaheim, USA, Sept. 1994.

[17] Chen, A. W.; Tinoco, E. N.
PAN AIR Application to Aero-Propulsion Integration
Jour. of Aircraft Vol. 21, No. 3, March 1984.

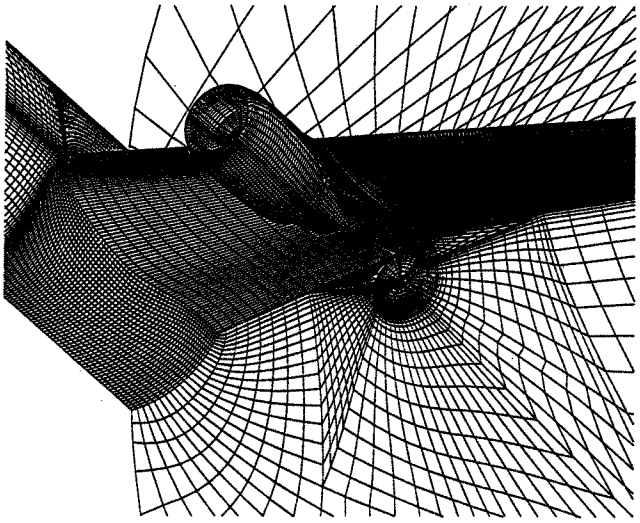

Figure 1: Global Grid

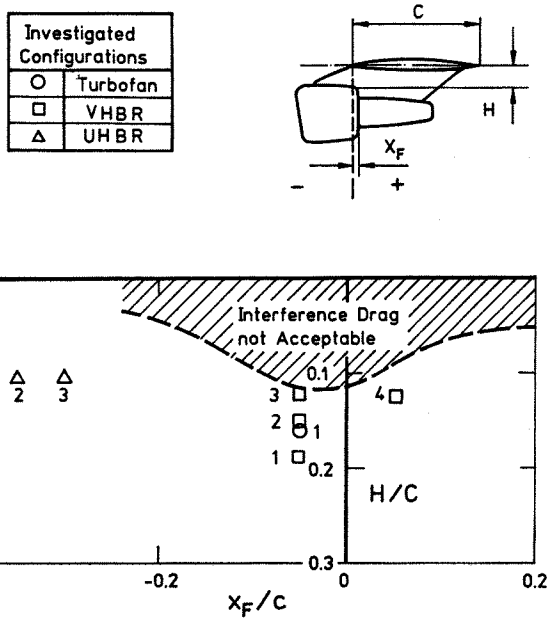

Figure 3: Engine Positions

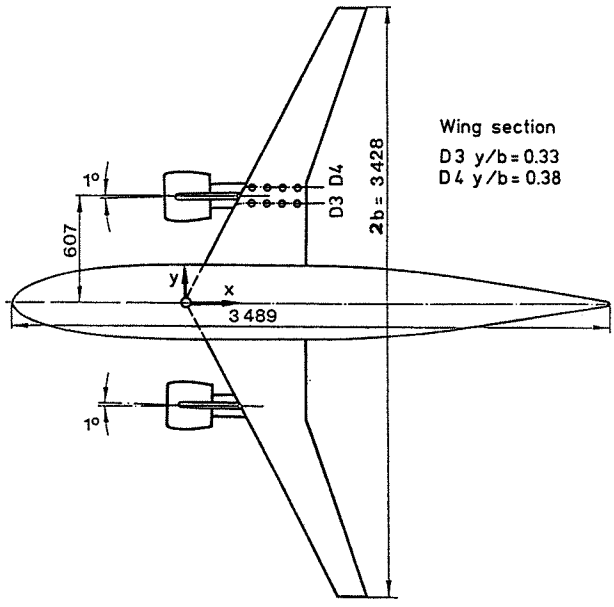

Figure 2: ALVAST Windtunnel Model

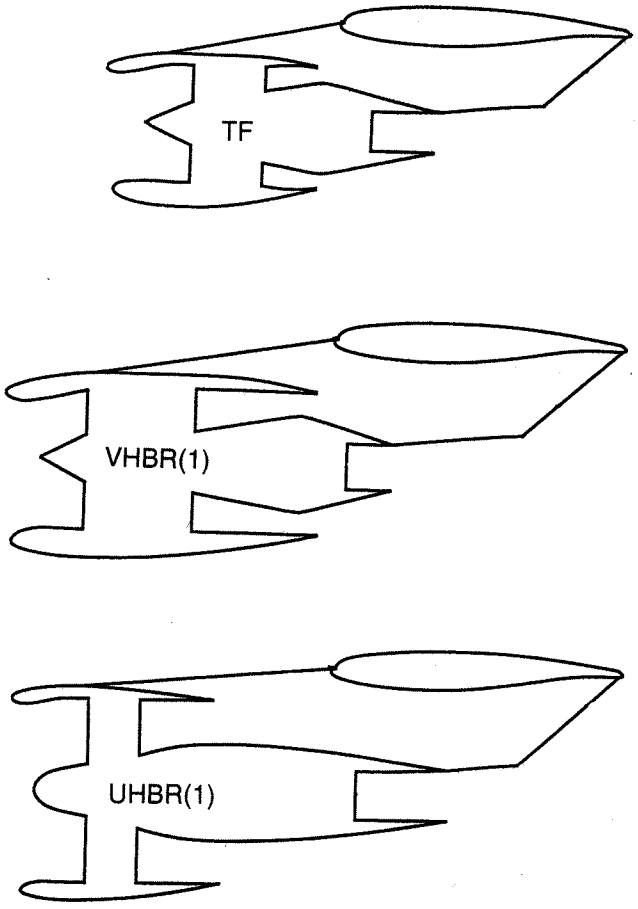

Figure 4: Sketch of Engines

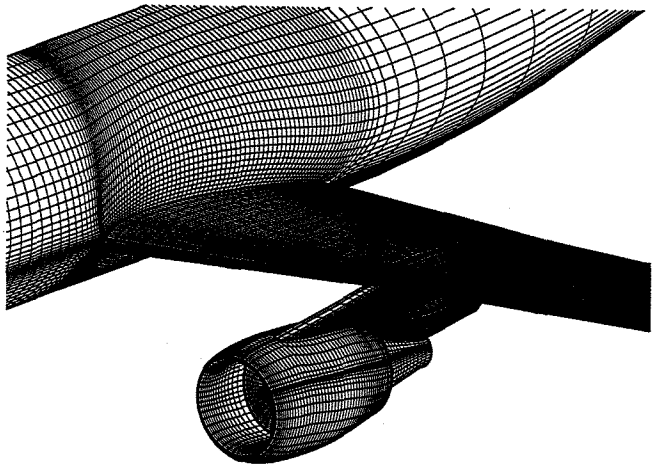

Figure 5a: Surface Grid TF

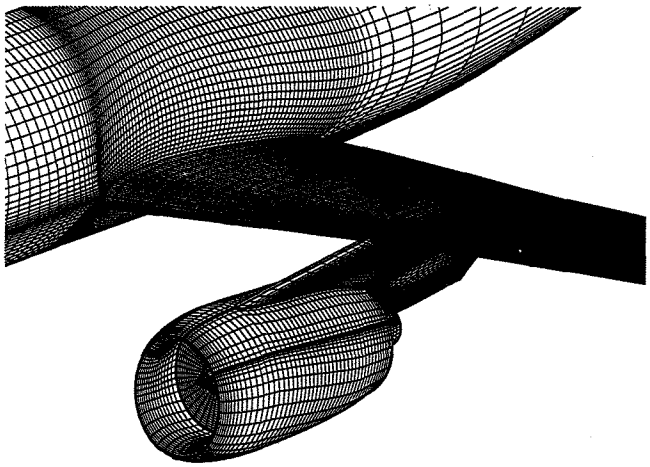

Figure 5b: Surface Grid VHBR

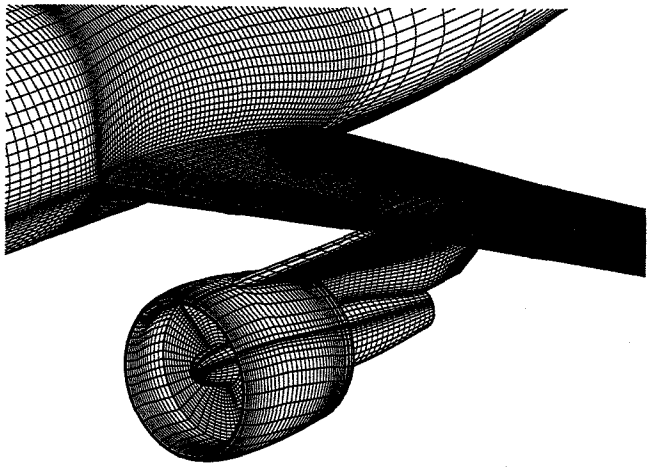

Figure 5c: Surface Grid UHBR

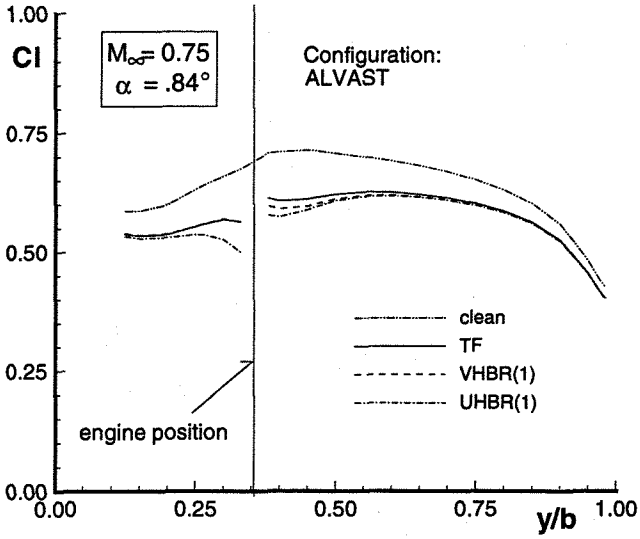

Figure 6: Wing Lift Distribution

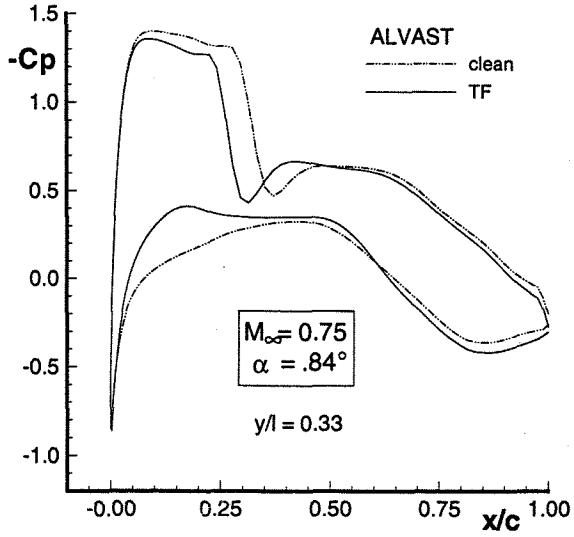

Figure 7a: Inboard Wing Pressure Distribution

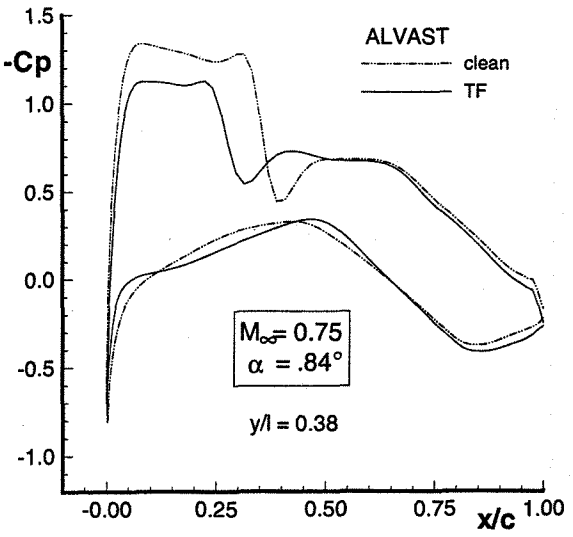

Figure 7b: Outboard Wing Pressure Distribution

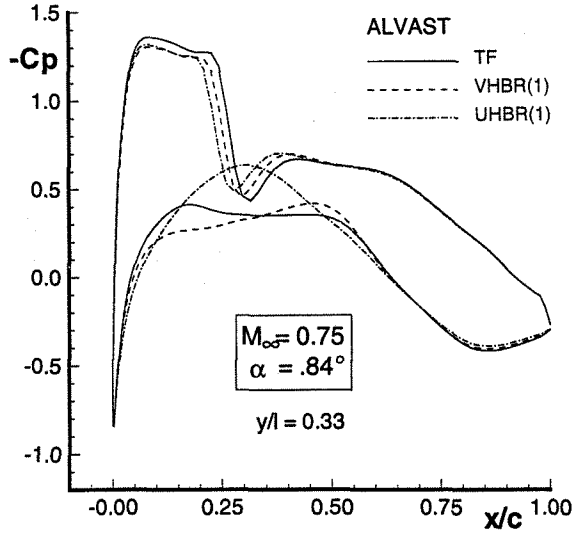

Figure 8a: Inboard Wing Pressure Distribution

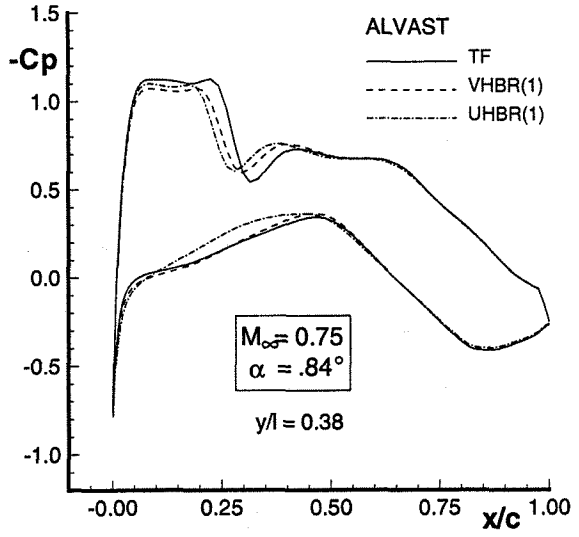

Figure 8b: Outboard Wing Pressure Distribution

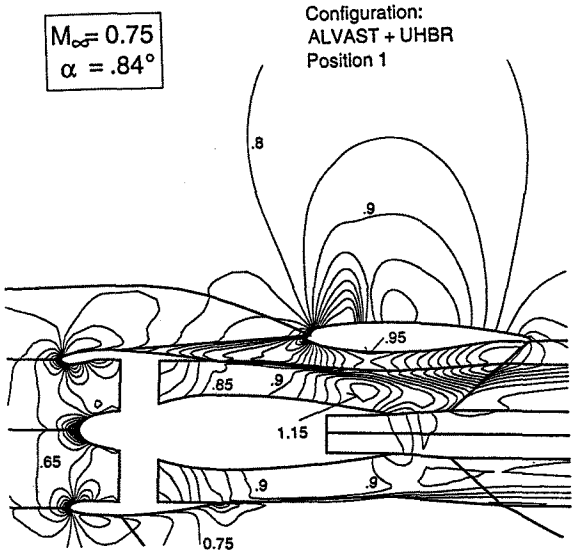

Figure 9: Machnumber Distribution (Inboard)

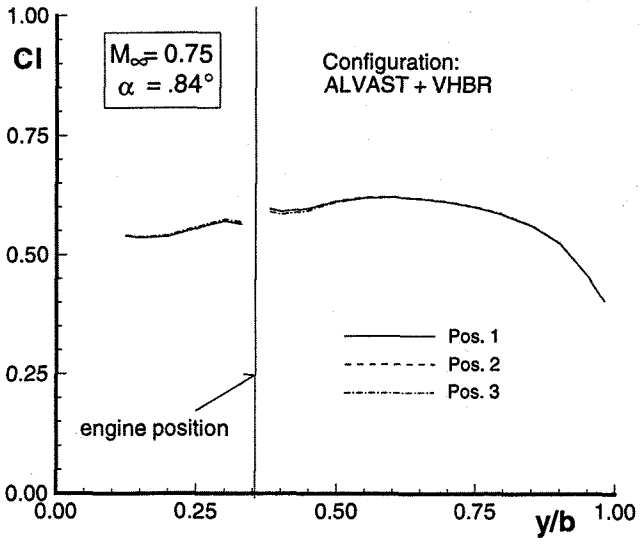

Figure 10: Wing Lift Distribution

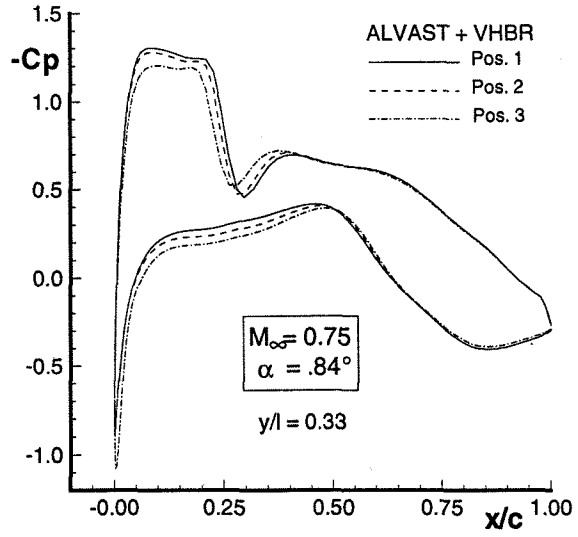

Figure 11a: Inboard Wing Pressure Distribution

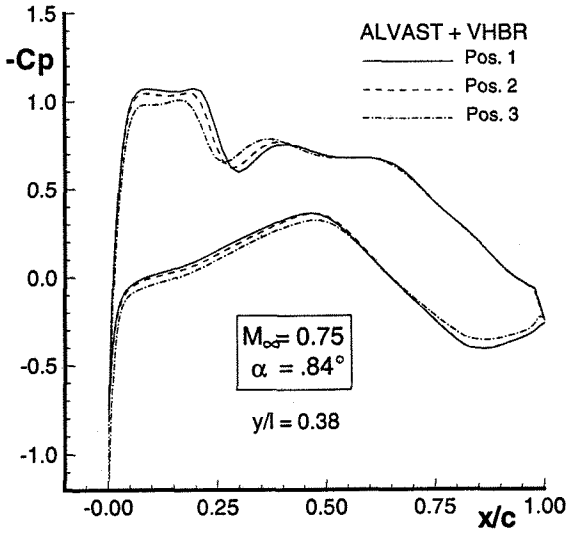

Figure 11b: Outboard Wing Pressure Distribution

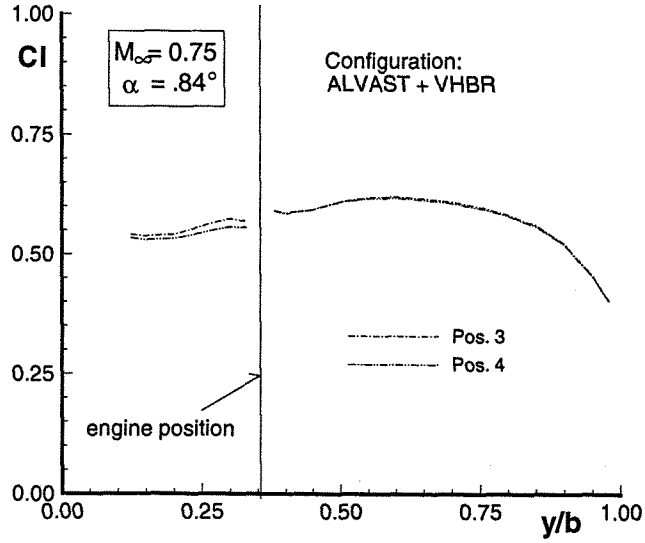

Figure 12: Wing Lift Distribution

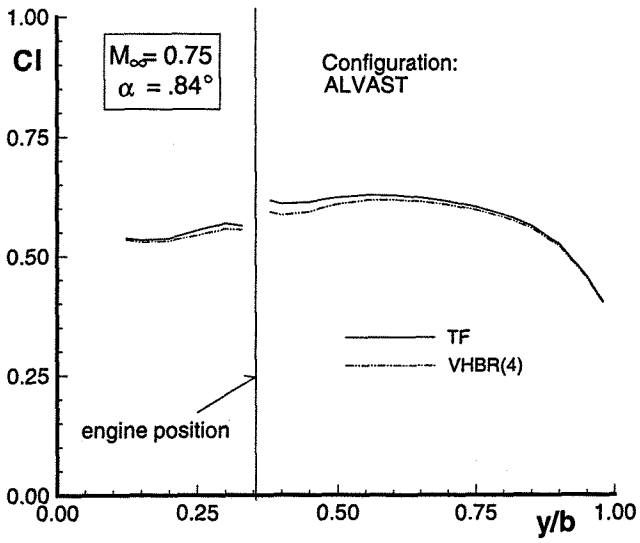

Figure 15: Wing Lift Distribution

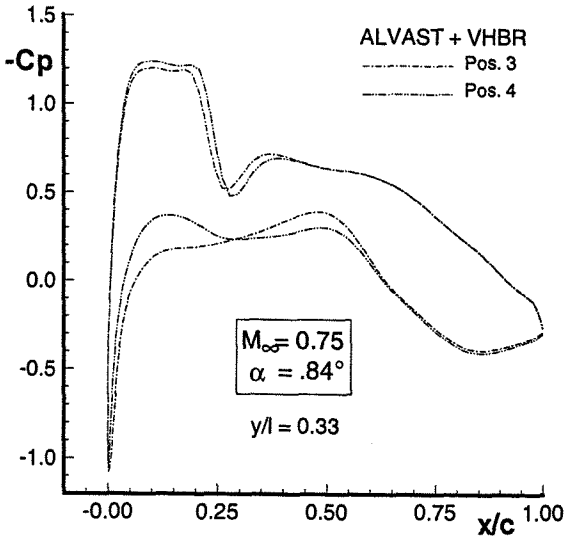

Figure 13a: Inboard Wing Pressure Distribution

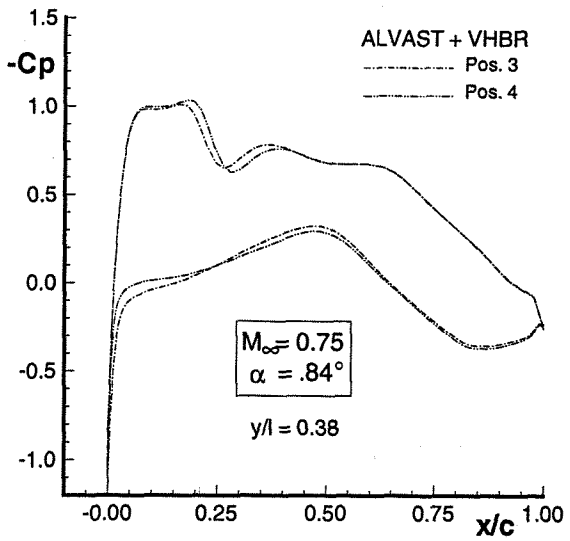

Figure 13b: Outboard Wing Pressure Distribution

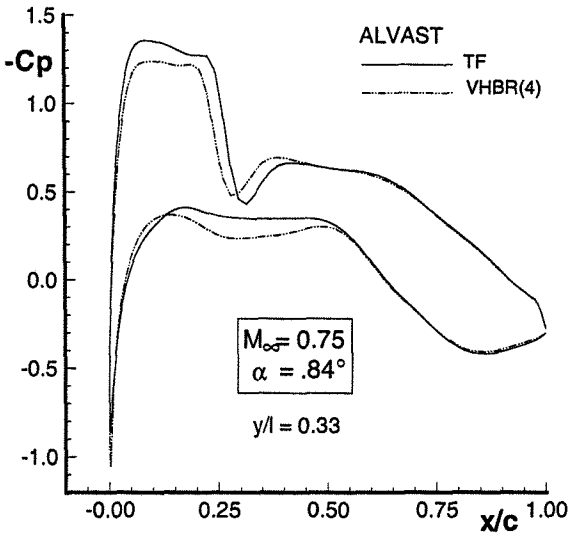

Figure 14a: Inboard Wing Pressure Distribution

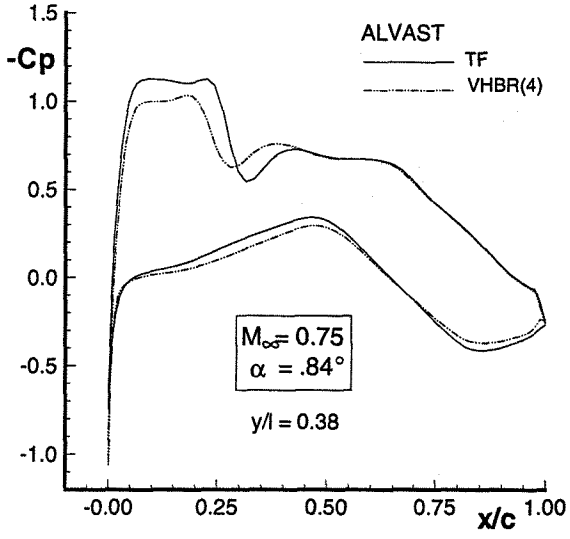

Figure 14b: Outboard Wing Pressure Distribution

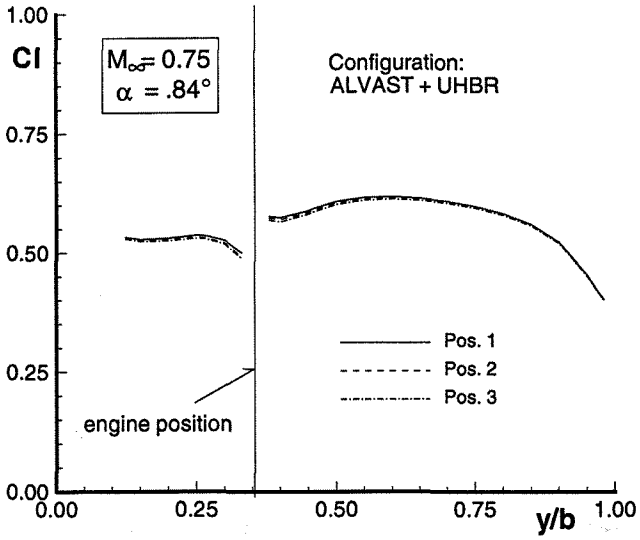

Figure 16: Wing Lift Distribution

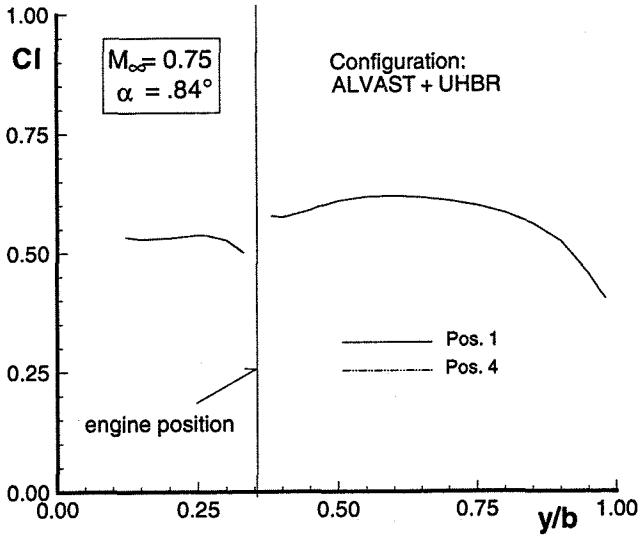

Figure 18: Wing Lift Distribution

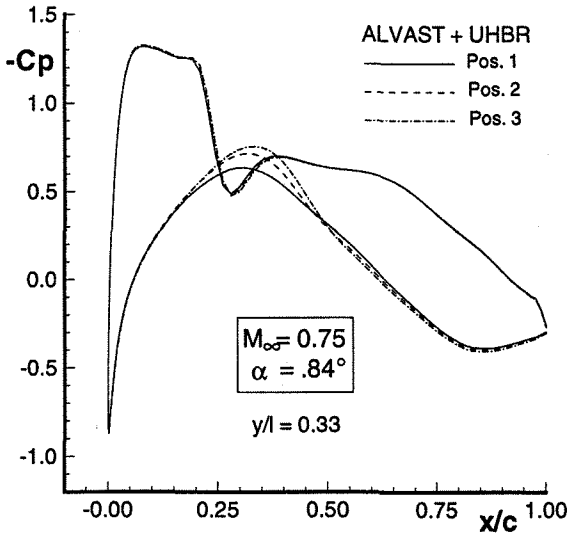

Figure 17a: Inboard Wing Pressure Distribution

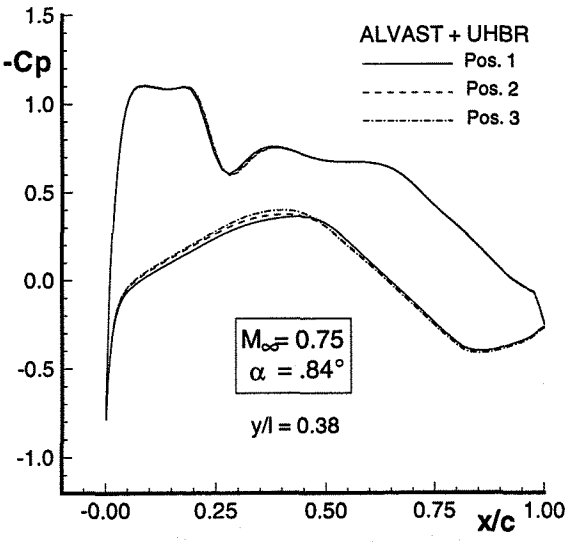

Figure 17b: Outboard Wing Pressure Distribution

Engine	TF	VHBR	UHBR
ε_{HL}	0.71	0.77	0.91
p_{tj}/p_o	2.0	1.9	1.7

Table 1: Engine Operating Conditions

	x_P/C	H/C	H_{axis}/C	Fan-Diameter/C
TF	-0.052	0.16	0.37	0.42
VHBR (1)	-0.052	0.19	0.43	0.51
VHBR (2)	-0.052	0.16	0.41	0.51
VHBR (3)	-0.052	0.12	0.37	0.51
VHBR (4)	+0.05	0.12	0.37	0.51
UHBR (1)	-0.41	0.11	0.43	0.65
UHBR (2)	-0.35	0.11	0.43	0.65
UHBR (3)	-0.30	0.11	0.43	0.65
UHBR (4)	-0.41	0.07	0.39	0.65

Table 2: Engine Positions